

Electric backaction on moiré mechanics

Héctor Ochoa 

*Donostia International Physics Center, 20018 Donostia-San Sebastian, Spain;
IKERBASQUE, Basque Foundation for Science, Maria Diaz de Haro 3, 48013 Bilbao, Spain;
and Department of Physics, Columbia University, New York, New York 10027, USA*

 (Received 12 December 2022; revised 21 March 2023; accepted 22 March 2023; published 21 April 2023)

A lattice mismatch between Van der Waals layers produces a moiré pattern and a subsequent electron band reconstruction. When the bilayer is charged, the sliding motion of one layer with respect to the other produces electric pumping. Here I discuss the reciprocal process: that a voltage bias produces a layer-shear mechanical force. The effect is deduced from the lowest-order correction to the mechanical action by the coupling with electrons in an external field. In twisted bilayer graphene the new mechanical force is shown to be perpendicular to the applied field (due to C_2 symmetries exchanging the layers) and proportional to the charge density measured from neutrality. This is strictly true when the chemical potential is within a gap opened by the moiré potential due to a topological quantization, and approximately true when the chemical potential crosses the flat bands in a model including the self-consistent Hartree interaction. In a mechanical device the effect should be manifested as an apparent enhancement of the friction between layers when the system is charged. Depinning fields for the sliding motion of the layers are estimated in the order of $\mathcal{E}_c \sim \text{kV/cm}$ around the magic angle.

DOI: [10.1103/PhysRevB.107.165417](https://doi.org/10.1103/PhysRevB.107.165417)

I. INTRODUCTION

The moiré patterns produced by a small lattice mismatch between Van der Waals layers reorganize their electronic spectrum in narrow bands defined on a smaller Brillouin zone. In twisted bilayer graphene [1] and other carbon-based structures with an emergent sixfold symmetry [2] this process is optimal at certain magic angles [3,4]. At low temperatures, the flat bands can host broken-symmetry phases and physics of correlated electrons yet to be understood [5–19]. The quantum geometry of the flat bands is likely to play a fundamental role, in particular, for the stability of the superconducting phase [20–22].

Another manifestation of geometrical phases of electrons in moiré patterns is the prediction of a charge pumping as the result of the translation of one layer with respect to the other [23–25] (see also Ref. [26]). For a bilayer with a threefold or sixfold principal axis (along \hat{z}), the pumped electric current density is related to the sliding velocity \mathbf{v} by

$$\mathbf{j} = C_{\parallel} \mathbf{v} + C_{\perp} \hat{z} \times \mathbf{v}, \quad (1)$$

where $C_{\parallel, \perp}$ are phenomenological parameters constrained by symmetry. For example, in the case of homobilayers where the moiré pattern results from a twist, additional twofold rotation axes within the plane of the device impose $C_{\parallel} = 0$. In the case of heterobilayers with no relative twist where the moiré pattern results from the difference in lattice parameters, additional mirror reflection planes containing \hat{z} yield $C_{\perp} = 0$.

As pointed out in Ref. [25], Eq. (1) is a general phenomenological relation that should be valid in any situation. Nevertheless, the topological character of this response is only manifest when the chemical potential lies within a gap opened by the moiré potential. The authors of Refs. [23–25] show independently that when the sliding motion is slow enough

compared to the timescale set by the inverse of the electronic gap twisted bilayer graphene realizes a two-dimensional (2D) analog of a Thouless pump [27].

Here, I provide a complementary discussion of this effect by focusing on the reciprocal process. I show that a voltage bias makes one layer to slide with respect to the other; more specifically, in the presence of an electromotive force \mathcal{E} there is a mechanical force (density) between layers of the form

$$\mathbf{f} = C_{\parallel} \mathcal{E} - C_{\perp} \hat{z} \times \mathcal{E}. \quad (2)$$

This relation is reciprocal to the pumping current in Eq. (1) and is, therefore, governed by the same phenomenological constants.

The structure of the paper is as follows. First, I will compute the correction to the mechanical action describing the dynamics of stacking configurations in the presence of an external field; this is Sec. II with some technical details relegated to appendices. In the limit of weak fields and smooth stacking fluctuations, the phenomenological parameters describing this coupling are given by integrals of the sliding Berry curvature introduced in Refs. [23–25]. These are evaluated for the continuum model of twisted bilayer graphene at the magic angle including also the effect of a self-consistent Hartree potential. The force is shown to be proportional to the charge density measured from neutrality, although this result is only rigorous when the chemical potential lies within a miniband gap (i.e., only when the adiabatic limit can be rigorously defined). I write general constitutive relations for the coupled charge and stacking dynamics and apply them to different experimental scenarios in Sec. III. This analysis shows that if the relative position of the layer is locked (for example, due to the presence of the contacts) there is still a negative correction to the electric polarization related to the mechanical deformation of the moiré pattern due to pinning forces

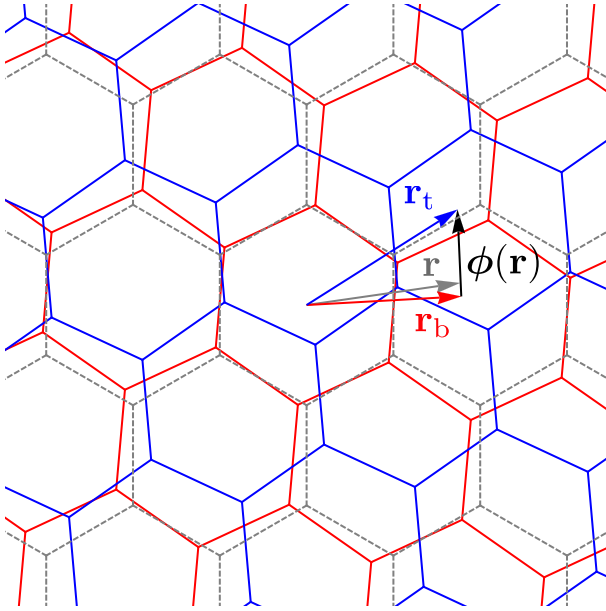


FIG. 1. Parametrization of stacking configurations. The field $\phi(\mathbf{r})$ relates a position \mathbf{r} in space with the local stacking configuration given as the relative translation of the layers that would generate the same configuration starting from maximum lattice overlap (AA stacking in graphene bilayers). Consider then a position \mathbf{r} (in gray) and its projections in the top (blue) and bottom (red) layers before the shift, in this case, a rigid rotation followed by a rigid translation of the layers; $\phi(\mathbf{r})$ is defined as the difference between the projections after the shift, $\phi(\mathbf{r}) = \mathbf{r}_t - \mathbf{r}_b$.

that contribute to partially screen the external field when the chemical potential is within a gap. The reciprocal effect is an apparent increase in the friction between layers when the moiré pattern slides, but charge cannot flow. Finally, I will show in Sec. IV that for weak disorder, the depinning fields for the sliding motion of the layers are estimated in $\mathcal{E}_c \approx 5$ kV/cm for magic-angle graphene. These are larger, for example, than the typical threshold fields for sliding conduction of charge density waves [28]. I will conclude in Sec. V with a discussion on the experimental viability of controlling the stacking order by the application of electric fields.

II. ADIABATIC FORCE ON STACKING ORDER

A. Preliminaries: Space of stacking configurations

The first assumption in the following derivation is that the electronic Hamiltonian of the bilayer in the absence of external fields only depends on positions through its parametric dependence on the local stacking configuration $\hat{\mathcal{H}}[\phi(\mathbf{r})]$, represented by the vector-valued field $\phi(\mathbf{r})$; see Fig. 1 for a definition. The sliding velocity introduced before measures the rate of changes in stacking configurations $\mathbf{v} = \delta\phi$. The important observation is that this space is periodic by construction: vectors ϕ and $\phi + \mathbf{R}$, where \mathbf{R} is a Bravais vector of graphene's lattice, represent the same stacking configuration.

The notion of a moiré period follows from this observation: At small twist angles and assuming no mismatch in

lattice constant the stacking field corresponding to a rigid rotation of angle θ can be approximated by $\phi_0(\mathbf{r}) \approx \theta \hat{\mathbf{z}} \times \mathbf{r}$ [29], and, hence, $\phi_0(\mathbf{r} + \mathbf{R}_m) = \phi_0 + \mathbf{R} \equiv \phi$ by construction, where $\mathbf{R}_m = \theta^{-1} \mathbf{R} \times \hat{\mathbf{z}}$ are the vectors of the moiré pattern in real space. More generally, the equilibrium stacking texture $\phi_0(\mathbf{r})$ (including lattice relaxation) describes a mapping between real space and the manifold of stacking configurations,

$$\phi_0(\mathbf{r}): \mathbf{r} \longrightarrow \phi \in S_1 \times S_1 \equiv T_2, \quad (3)$$

which possesses the topology of a torus. The simplest mechanism for the mechanical force in Eq. (2) is related to the accumulation of geometrical phases by the electronic wave function along a nontrivial loop defined on this space.

B. Effective action

The dynamics of the stacking field $\phi(t, \mathbf{r})$ is governed by the Lagrangian

$$\mathcal{L}_{\text{mech}}[\phi(t, \mathbf{r})] = \frac{\varrho_\phi}{2} \int d\mathbf{r} \dot{\phi}^2 - \mathcal{U}[\phi(t, \mathbf{r})], \quad (4)$$

where $\mathcal{U}[\phi(t, \mathbf{r})]$ is the mechanical free energy of the bilayer and ϱ_ϕ parametrizes the inertia of the relative motion of the two layers, hence, $\varrho_\phi = \varrho/2$, where ϱ is the areal mass density of each layer.

The form of \mathcal{U} is not relevant for the following discussion, but it consists essentially of two competing terms, one accounting for the adhesion forces between layers favoring certain stacking configurations, and the other penalizing intralayer stress. The equilibrium stacking texture $\phi_0(\mathbf{r})$ is the result of the minimization of \mathcal{U} subjected to a boundary condition that stabilizes the twist angle θ . Putting aside the important question of the stability of the angle as the layers slide, I will consider then the dynamics around this equilibrium solution, $\phi(t, \mathbf{r}) = \phi_0(\mathbf{r}) + \delta\phi(t, \mathbf{r})$. In particular, we are interested in the slow sliding dynamics of the bilayer assuming that the layers are free to slide, i.e., that the layers are incommensurate to each other so that the sliding motion adiabatically connects isoenergetic stacking configurations involving no distortion of the moiré pattern. The local change in stackings is of the form $\delta\phi(t, \mathbf{r}) = \phi_0(\mathbf{r} - \mathbf{u}(t)) - \phi_0(\mathbf{r})$, where $\mathbf{u}(t)$ corresponds to the collective coordinate associated with soft collective modes (phasons) in the spectrum of stacking fluctuations [30–35]. If we neglect lattice relaxation, this is just a rigid translation of one layer with respect to the other. More generically, it parametrizes the traveling wave associated with the sliding motion of stacking domain walls resulting from the relaxation process.

The goal here is to compute the correction to the mechanical action in the presence of external fields. We start with the action for electrons in the bilayer coupled to a scalar (V) and vector (\mathbf{A}) potentials,

$$S[\psi, \psi^\dagger] = \int dt \int d\mathbf{r} \psi^\dagger (i\hbar\partial_t + eV + \mu - \hat{\mathcal{H}}[\phi, \mathbf{A}])\psi, \quad (5)$$

where μ is the chemical potential. The vector potential enters in minimal coupling, $-i\hbar\partial \rightarrow -i\hbar\partial + e\mathbf{A}/c$. We can formally integrate out electrons, $iS_{\text{eff}}[\phi]/\hbar = \text{Tr} \ln \hat{\mathcal{G}}[\phi]$, to produce an effective action for stacking configurations through the

parametric dependence of the Hamiltonian; here, $\hat{\mathcal{G}}[\boldsymbol{\phi}] = (i\hbar\partial_t + eV + \mu - \hat{\mathcal{H}}[\boldsymbol{\phi}, \mathbf{A}])^{-1}$, and the trace represents the summation over all quantum numbers.

Since we are interested only in the force produced on the stacking order in linear response to the external fields, we can consider the linear correction to the electronic Hamiltonian in stacking deviations, $\hat{\mathcal{H}}[\boldsymbol{\phi}, \mathbf{A}] \approx \hat{\mathcal{H}}_0[\mathbf{A}] + \delta\boldsymbol{\phi} \cdot \partial_{\boldsymbol{\phi}}\hat{\mathcal{H}}$, where $\hat{\mathcal{H}}_0[\mathbf{A}] \equiv \hat{\mathcal{H}}[\boldsymbol{\phi}_0, \mathbf{A}]$, and expand the logarithm up to first order both in the $\delta\boldsymbol{\phi}$ and the fields. Diagrammatically, this amounts to the calculation of the usual polarization bubble but with the coupling $\partial_{\boldsymbol{\phi}}\hat{\mathcal{H}}$ in the vertex with $\delta\boldsymbol{\phi}$. The stacking configurations are assumed to be smoothly varying in space and time, so we can expand the polarization to first order in the external frequency/momentum. This produces the following correction in the effective action:

$$S_{\text{eff}}^{(2)}[\delta\boldsymbol{\phi}] = \tilde{C}_{ij} \int dt \int d\mathbf{r} \left(eV \partial_i \delta\phi_j + \frac{e}{c} A_i \delta\dot{\phi}_j \right), \quad (6)$$

where repeated indices are summed up, and the coefficients \tilde{C}_{ij} have the form of a Pontryagin index,

$$\tilde{C}_{ij} = \int \frac{dq}{(2\pi)^3} \text{Tr}[\hat{\mathcal{G}}_0 \cdot \partial_\omega \hat{\mathcal{G}}_0^{-1} \cdot \hat{\mathcal{G}}_0 \cdot \partial_{q_j} \hat{\mathcal{G}}_0^{-1} \cdot \hat{\mathcal{G}}_0 \cdot \partial_{q_i} \hat{\mathcal{G}}_0^{-1}], \quad (7)$$

with $q = (\omega, \mathbf{q})$. Here, I have introduced the *free* Green's operator in the absence of external fields,

$$\hat{\mathcal{G}}_0(\omega, \mathbf{q}) = [\hbar\omega + i0^+ \text{sgn}(\omega) + \mu - \hat{\mathcal{H}}_0(\mathbf{q})]^{-1}, \quad (8)$$

where $\hat{\mathcal{H}}_0(\mathbf{q})$ is the Fourier transform of the electronic Hamiltonian defined as a matrix spanned by band indices and with momenta \mathbf{q} restricted to the moiré Brillouin zone (mBZ).

From this term in the action, we see that the field produces a force (density) of the form

$$\mathbf{f} = \frac{\delta S_{\text{eff}}^{(2)}}{\delta \boldsymbol{\phi}} = \hat{C}^T \cdot \boldsymbol{\mathcal{E}}, \quad (9)$$

where $\boldsymbol{\mathcal{E}} = -\nabla V - \dot{\mathbf{A}}/c$ is the electric field and \hat{C} is a matrix with elements $C_{ij} = e\tilde{C}_{ij}$. This is nothing but Eq. (2). The symmetry constraints discussed in the Introduction follows from the symmetry transformations of momentum and stacking fields. Both are vectors, but note, in particular, that they have opposite signatures with respect to operations exchanging the layers.

By the same token, there is a contribution to the electric current (density) given by

$$\mathbf{j} = c \frac{\delta S_{\text{eff}}^{(2)}}{\delta \mathbf{A}} = \hat{C} \cdot \delta\dot{\boldsymbol{\phi}}, \quad (10)$$

which is another way to write Eq. (1). The constants C_{ij} are the same in both expressions, but the corresponding matrices are transposed.

Finally, performing the integral in frequencies in Eq. (7) (see Appendix A), the response coefficients can be written as

$$C_{ij} = e \sum_{\alpha, n} \int_{\text{mBZ}} \frac{d\mathbf{q}}{(2\pi)^2} \Omega_{q_i, \phi_j}^{(n, \alpha)}(\mathbf{q}) \Theta[\mu - \varepsilon_{n, \alpha}(\mathbf{q})], \quad (11)$$

where $\Omega_{q_i, \phi_j}^{(n, \alpha)}(\mathbf{q})$ the sliding Berry curvature introduced in Refs. [23–25] summed over all occupied states with energy

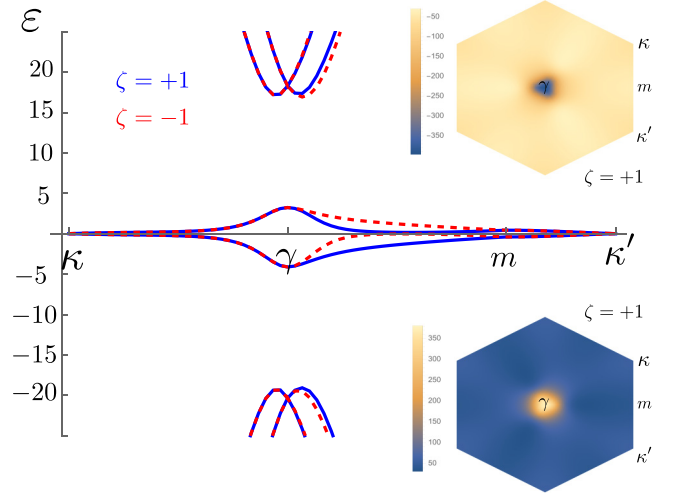


FIG. 2. Flat bands and sliding Berry curvatures at the magic angle. The insets show the distribution in momentum space of $\Omega_{\perp}^{(n, +)}(\mathbf{q})$ in Eq. (14) summed over occupied bands when the highest flat band is fully occupied (top) and when the lowest flat band is fully empty (bottom). I truncated the continuum Hamiltonian to 91 plane waves for each layer and sublattice.

dispersion $\varepsilon_{n, \alpha}(\mathbf{q})$ (n is the band index, and α represents the rest of the quantum numbers).

C. Application to twisted bilayer graphene

1. Noninteracting bands

Next, I evaluate the matrix of coefficients C_{ij} within the continuum model of the twisted bilayer graphene [1,4]. The model consists of two Dirac Hamiltonians describing the original linear dispersion of the bands on each layer at valleys centered at the two inequivalent points $\mathbf{K}_{\pm} = \pm\mathbf{K}_{+}$ of the hexagonal Brillouin zone. Tunneling from the bottom to the top layer is described by the term

$$\hat{T}_{\zeta}(\mathbf{r}) = \sum_{n=0}^2 e^{i\zeta(\mathbf{q}_n + \mathbf{K}_{+}) \cdot \boldsymbol{\phi}(\mathbf{r})} e^{i\zeta \frac{2\pi n}{3} \hat{\sigma}_z} \hat{T}_0 e^{-i\zeta \frac{2\pi n}{3} \hat{\sigma}_z}, \quad (12)$$

where $\zeta = \pm 1$ labels valleys \mathbf{K}_{\pm} , and $\mathbf{q}_{0,1,2} = \mathbf{0}, \mathbf{g}_2, -\mathbf{g}_1$, where $\mathbf{g}_{1,2}$ are primitive vectors of graphene's reciprocal lattice forming 120° . Operators $\hat{\sigma}_i$ are Pauli matrices acting on the sublattice degree of freedom of the spinor wave functions. The matrix \hat{T}_0 contains the tunneling rates; a parametrization compatible with D_6 symmetry is of the form

$$\hat{T}_0 = t_{AA} \hat{1} + t_{AB} \hat{\sigma}_x. \quad (13)$$

Plugging $\boldsymbol{\phi}_0(\mathbf{r}) \approx \theta \hat{\mathbf{z}} \times \mathbf{r}$ into these equations one recovers the usual expression of the continuum model with moiré reciprocal vectors given by $\mathbf{G}_i = \theta^{-1} \mathbf{g}_i \times \hat{\mathbf{z}}$. Lattice relaxation produces more harmonics, but I will neglect those and take slightly different values of the interlayer tunneling rates at different stacking regions, $t_{AA} = 79.7$ and $t_{AB} = 97.5$ meV [36]. Figure 2 shows the lowest-energy bands at the magic angle ($\theta = 1.05^\circ$ for these model parameters) including up to 91 plane waves in the calculation for each layer and sublattice.

As discussed in the Introduction, D_6 symmetry imposes $C_{xx} = C_{yy} = 0$ and $C_{yx} = -C_{xy} \equiv C_{\perp}$, the latter given by the integral of the corresponding component of the sliding Berry curvature. The insets in Fig. 2 show the distribution of the symmetric combination,

$$\Omega_{\perp}^{(n,\zeta)}(\mathbf{q}) = \frac{1}{2}\Omega_{q_y\phi_x}^{(n,\zeta)}(\mathbf{q}) - \frac{1}{2}\Omega_{q_x\phi_y}^{(n,\zeta)}(\mathbf{q}), \quad (14)$$

for valley $\zeta = +1$, summed over the 182 bands below the flat bands (lower inset), and including also the flat bands (upper inset). The distribution in the opposite valley follows from time-reversal symmetry, $\Omega_{\perp}^{(n,-)}(\mathbf{q}) = \Omega_{\perp}^{(n,+)}(-\mathbf{q})$. Summing $\Omega_{\perp}^{(n,+)}(\mathbf{q})$ on a grid of 1933 \mathbf{q} points and accounting for the degeneracy 4 from spin and valley, I obtained $A_m C_{\perp}/4e = 56.31$ for the lower inset and $A_m C_{\perp}/4e = -56.52$ for the upper inset ($A_m = \sqrt{3}a^2/2\theta^2$ is the area of the moiré unit cell in real space, where a is graphene's lattice constant). These are numerically very close to $\pm\theta^{-1} = \pm 54.57$. Indeed, I checked that the force coefficient follows the relation $C_{\perp} = \pm 4e/\theta A_m$ for different values of twist angle within the same numerical error (results not shown); in terms of the electron density n measured from neutrality,

$$C_{\perp} = -\theta^{-1}en = -\frac{8e\theta}{\sqrt{3}a^2}. \quad (15)$$

The same estimate (with opposite sign) follows for hole dopings.

2. Hartree bands

As it is apparent from the insets in Fig. 2 most of the sliding Berry curvature of the flat bands is concentrated around the zone center (γ point in the figures), so C_{\perp} does not necessarily track the carrier density as the flat bands are gradually populated. However, it is well known that electrostatic effects alter significantly the dispersion of the flat bands as charge is added or removed from the bilayer [37–40]. In order to investigate charging effects in the bands and the distribution of sliding Berry curvature, I included in the electronic Hamiltonian the Coulomb repulsion among electrons treated in a self-consistent Hartree approximation. Details can be found in Appendix B. The Fock terms (neglected here) give rise to exchange renormalizations of the bands and symmetry breaking at low temperatures, but, being nonlocal potentials, they are less sensitive to the accumulation of charge in some areas of the moiré pattern and, therefore, they are expected to have a smaller effect on the distribution of the sliding Berry curvature and the force coefficients.

Figure 3 shows the self-consistent Hartree band structures corresponding to a long-range Coulomb interaction with a relative permittivity $\epsilon_r = 7.5$ for fully empty [panel (a)] and fully occupied [panel (b)] flat bands. The density plots represent $\Omega_{\perp}^{(n,+)}(\mathbf{q})$ summed over all filled bands for each filling. The sum in the same momentum grid as before gives $A_m C_{\perp}/4e = 55.66$ for filling $\nu = -4$ and $A_m C_{\perp}/4e = -55.69$ for filling $\nu = 4$.

3. C_{\perp} as a function of band filling

The calculations in Fig. 3 show that the sliding Berry curvature with the account of the Hartree potential is, in fact,

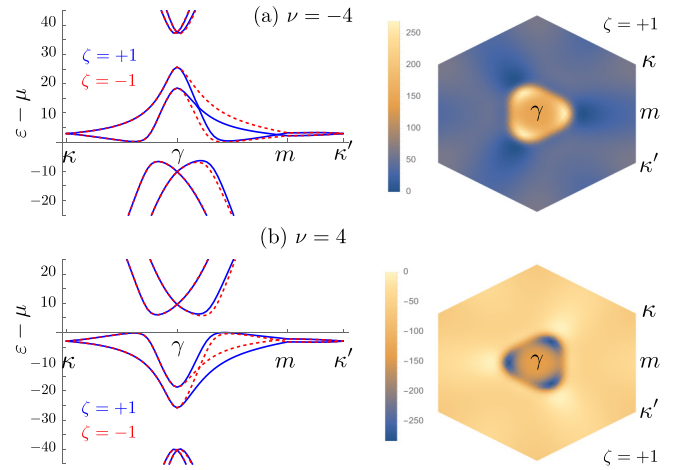


FIG. 3. Hartree bands and sliding Berry curvature. The dielectric constant is $\epsilon_r = 7.5$. I took the same number of plane waves as in the calculations in Fig. 2, and the harmonics of the Hartree potential were restricted to the first star. (a) Filling $\nu = -4$ when the chemical potential lies within the gap between the lowest flat band and the rest of the spectrum. The right panel shows $\Omega_{\perp}^{(n,+)}(\mathbf{q})$ summed over all occupied bands. (b) Filling $\nu = 4$ when the chemical potential lies within the gap between the highest flat band and the rest of the spectrum. The right panel shows $\Omega_{\perp}^{(n,+)}(\mathbf{q})$ summed over all occupied bands.

more spread over the moiré Brillouin zone. How do these changes affect the value of C_{\perp} as the Fermi level crosses the flat bands? Here, I am concerned only about the magnitude of the reactive force induced by the field, although in the presence of a Fermi surface the adiabatic limit cannot be properly defined and we should expect also dissipative terms due to electron quasiparticle excitations.

The answer is in Fig. 4, which shows the numerical evaluation of C_{\perp} as a function of filling ν running from -4 (completely empty flat bands) to $+4$ (completely full). The

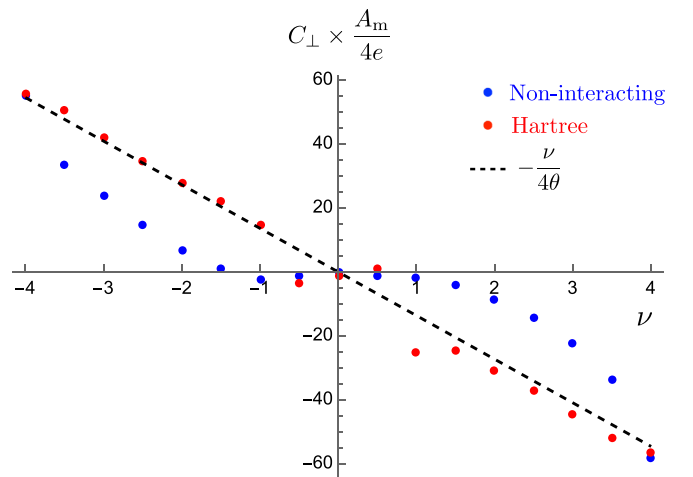


FIG. 4. C_{\perp} as a function of filling of the flat bands. Blue dots correspond to the noninteracting theory, red dots to the self-consistent Hartree theory. The dashed black line corresponds to C_{\perp} tracking the charge density.

blue dots correspond to the rigid noninteracting bands in which C_{\perp} decreases rapidly as the lowest flat band starts to be populated, then it is roughly 0 for a wide range of densities around the neutrality point, and then decreases quickly again.

However, for the nonrigid Hartree bands, which change with filling, the behavior is different; these correspond to the red points in Fig. 4. We can see that C_{\perp} is roughly proportional to band filling (dashed black line for reference) except for a much narrower window around neutrality. This is the result of the ν -dependent change in band dispersion associated with the smoothening of the charge density in real space together with the spreading of the sliding Berry curvature in reciprocal space.

4. Coupled charge and twist-angle fluctuations

The quantization of C_{\perp} in units of $e/\theta A_m$ when the Fermi level lies within a gap can be understood by rewriting Eq. (11) in terms of the four Chern numbers defined on manifolds $S_1 \times S_1$ spanned by a primitive vector of the moiré Brillouin zone and a primitive vector of the stacking configuration space [23–25]; the derivation is shown in Appendix C. Physically, the integral of the sliding Berry curvature describes how the Wannier center of the band changes with stacking, so C_{\perp} tracks the charge density in the adiabatic limit.

Another way to understand the relation between C_{\perp} and band filling is the following relation for the charge density fluctuation associated with spatial variations of the stacking configuration. From the effective action we have

$$\delta n = -\frac{\delta S_{\text{eff}}^{(2)}}{\delta V} = -C_{ij}\partial_i\delta\phi_j = C_{\perp}(\nabla \times \delta\boldsymbol{\phi})_z. \quad (16)$$

This relation is complementary to the expression of the pumping current, in the sense that the gauge invariance of the new term in the effective action guarantees that the pumped current is conserved, $\delta\dot{n} + \nabla \cdot \mathbf{j} = 0$.

If we compare the right-hand side with the stacking texture for a rigid rotation $\boldsymbol{\phi}_0(\mathbf{r}) \approx \theta\hat{\mathbf{z}} \times \mathbf{r}$, then we can read Eq. (16) as a relation between adiabatic changes in the charge distribution and smooth (on the scale of the moiré pattern) spatial variations of the twist angle: $(\nabla \times \delta\boldsymbol{\phi})_z \approx 2\delta\theta$, hence, $\delta n = 2C_{\perp}\delta\theta$. On the other hand, for a fixed filling we can write $n = -e\nu/A_m \propto \theta^2$. A smooth change in twist angle modifies the area of the moiré cell and, thus, the density, $\delta n = \delta\theta\delta_{\theta}n = 2n\delta\theta/\theta$. Comparing both expressions we expect then $C_{\perp} = n/\theta = -e\nu/\theta A_m$, which agrees with Eq. (15) for full fillings $\nu = \pm 4$.

III. CONSTITUTIVE RELATIONS

The purpose of this section is twofold: First, I will show that regardless of its microscopic origin, the force in Eq. (2) follows from the phenomenological expression for the pumping current in Eq. (1) as a result of Onsager reciprocity. Then, I will apply the constitutive relations to different experimental scenarios.

A. Mechanical force from Onsager reciprocity

The procedure is to write general constitutive relations describing the coupled charge and sliding dynamics of the

bilayer. These expressions relate flows with their conjugate thermodynamic forces via a matrix of linear-response functions. The product of the flows with their conjugated forces determine the work that we have to supply in order to sustain transport. When charge flows and one of the layers slides the work dissipated per unit of area is

$$\Delta\bar{W} = \int_{-\infty}^{\infty} \frac{d\omega}{2\pi} [\mathbf{j}^*(\omega) \cdot \boldsymbol{\mathcal{E}}(\omega) + \mathbf{v}^*(\omega) \cdot \mathbf{f}(\omega)]. \quad (17)$$

Here, I have introduced Fourier transforms in time of currents and forces. From this expression, we identify the electric field $\boldsymbol{\mathcal{E}}$ as the thermodynamic force conjugate to the electric current. The force conjugate to the sliding velocity is simply $\mathbf{f} = -\delta\mathcal{U}/\delta\boldsymbol{\phi}$. In linear response, we write

$$\begin{bmatrix} \mathbf{j}(\omega) \\ \mathbf{v}(\omega) \end{bmatrix} = \begin{bmatrix} \hat{\sigma}(\omega) & \hat{A}(\omega) \\ \hat{B}(\omega) & -i\omega\hat{\chi}(\omega) \end{bmatrix} \begin{bmatrix} \boldsymbol{\mathcal{E}}(\omega) \\ \mathbf{f}(\omega) \end{bmatrix}. \quad (18)$$

Thermodynamic stability requires that the real part of this block matrix is positive semidefinite. Time-reversal symmetry dictates that it must be symmetric; in particular,

$$\hat{B}(\omega) = \hat{A}^T(\omega). \quad (19)$$

In the $\omega = 0$ limit this property reduces to the Onsager reciprocal relations among transport coefficients.

Before jumping into the off-diagonal blocks containing $C_{\parallel,\perp}$, it is worth discussing the diagonal blocks for a moment. In the charge sector $\mathbf{j}(\omega)$ and $\boldsymbol{\mathcal{E}}(\omega)$ are related by the optical conductivity $\hat{\sigma}(\omega)$. In the mechanical sector, sliding velocities and forces are related by the long-wavelength ($\mathbf{q} = 0$) limit of the stacking susceptibility tensor $\hat{\chi}(\omega, \mathbf{q})$ introduced in Ref. [33]. For the purposes of DC transport, we only need to capture the behavior at small frequencies, which is dominated by the phason modes [30–35] discussed before. We can write then [33],

$$\hat{\chi}(\omega, \mathbf{q}) = \sum_{\nu=L,T} \frac{e_{\phi}^{-1}\hat{P}_{\nu,\mathbf{q}}}{\omega_{\nu,\mathbf{q}}^2 - \omega^2 - i\omega\gamma_{\nu}(\omega, \mathbf{q})}, \quad (20)$$

where $\hat{P}_{\nu,\mathbf{q}}$ are projectors on the space of phason modes labeled by momentum \mathbf{q} within the moiré Brillouin zone (in a continuum elastic theory that assumes moiré translational invariance) and branch indices $\nu = L, T$. These modes correspond to longitudinal (L) and transverse (T) traveling waves of the moiré pattern. They are soft in the sense that $\omega_{\nu,\mathbf{q}} \rightarrow 0$ as $\mathbf{q} \rightarrow 0$ due to incommensurability (or negligible energy differences between commensurate and incommensurate structures at small twist angles). Finally, $\gamma_{\nu}(\omega, \mathbf{q})$ is a memory matrix that introduces the effect of harder modes of the stacking dynamics. The $\omega = 0, \mathbf{q} = 0$ limit of the memory matrix is a kinetic coefficient describing the friction between the two layers. It can be written as a Green's-Kubo formula of the form [33]

$$\begin{aligned} \gamma &\equiv \lim_{\omega \rightarrow 0} \lim_{\mathbf{q} \rightarrow 0} \gamma_{\nu}(\omega, \mathbf{q}) \\ &= \frac{1}{k_B T} \lim_{\epsilon \rightarrow 0^+} \lim_{\mathbf{q} \rightarrow 0} \int_0^{\infty} dt e^{-\epsilon t} \langle f_{\nu}(t, \mathbf{q}) f_{\nu}(0, \mathbf{q}) \rangle_T, \end{aligned} \quad (21)$$

where I have introduced equilibrium correlation functions between microscopic forces $f_{\nu}(t, \mathbf{q})$ acting on mode (ν, \mathbf{q}) .

The important observation is that the effect of these fluctuating forces is finite at $\mathbf{q} = 0$ due to anharmonic coupling with optical phonons, reflecting that the linear momentum of an individual layer is not conserved; γ is its characteristic relaxation rate. Consequently, under the application of a mechanical force the layer slides at some finite velocity in the steady state; otherwise, the layer would accelerate infinitely. From the spectral point of view, this means that phasons are overdamped at long wavelengths [33].

Consider first the pumping scenario, i.e., the flow of electric charge due to a mechanical force in the absence a voltage bias, $\mathcal{E}(\omega) = 0$. In this case, the constitutive relations dictate

$$\mathbf{j}(\omega) = \hat{A}(\omega) \cdot \mathbf{f}(\omega), \quad (22a)$$

$$\mathbf{v}(\omega) = -i\omega \hat{\chi}(\omega) \cdot \mathbf{f}(\omega). \quad (22b)$$

Note that the $\omega = 0$ limit in the second relation reads $\mathbf{v}(0) = \mathbf{f}(0)/\gamma\varrho$, i.e., one layer slides at the velocity imposed by the applied force compensated by the friction with the other layer. Combining both equations, we have

$$\mathbf{j}(\omega) = \frac{i}{\omega} \hat{A}(\omega) \cdot \hat{\chi}^{-1}(\omega) \cdot \mathbf{v}(\omega). \quad (23)$$

Comparing Eq. (1) with this last equation, we conclude that at small frequencies $\hat{A}(\omega)$ should go as

$$A_{ij}(\omega) = \frac{\varrho_\phi^{-1}}{\gamma - i\omega} (C_{\parallel} \delta_{ij} - C_{\perp} \epsilon_{ij}). \quad (24)$$

Now we consider the reciprocal effect, i.e., the sliding of one layer with respect to the other due to a voltage bias in the absence of a mechanical force, $\mathbf{f}(\omega) = 0$. By making use of the last result along with Onsager reciprocity [Eq. (19)], the constitutive relations dictate

$$\mathbf{v}(\omega) = \frac{\varrho_\phi^{-1}}{\gamma - i\omega} (C_{\parallel} - C_{\perp} \hat{\mathbf{z}} \times) \mathcal{E}(\omega). \quad (25)$$

The electric field makes the layers slide as if they were subjected to the shear force \mathbf{f} in Eq. (2). Alternatively, in the presence of a bias voltage, if the layers do not slide there must be a mechanical force opposing Eq. (2) so that the relative position of the layers remains locked. We will come back to this scenario later.

Finally, note that thermodynamic stability imposes the following relation between transport coefficients,

$$\frac{\gamma \varrho_\phi}{\rho} \geq C_{\parallel}^2 + C_{\perp}^2, \quad (26)$$

where $\rho = \sigma^{-1}(0)$ is the electric resistivity.

B. Experimental scenarios

Let us consider first the scenario in which the device geometry (due to the contacts, encapsulation, etc.) prevents the two layers to move with respect to each other, $\mathbf{v}(\omega) = 0$. The constitutive relations dictate

$$\mathbf{j}(\omega) = \hat{\sigma}(\omega) \cdot \mathcal{E}(\omega) + \frac{C_{\parallel} + C_{\perp} \hat{\mathbf{z}} \times}{\gamma \varrho_\phi (1 - i\omega \gamma^{-1})} \mathbf{f}(\omega), \quad (27a)$$

$$(C_{\parallel} - C_{\perp} \hat{\mathbf{z}} \times) \mathcal{E}(\omega) + \mathbf{f}(\omega) = 0. \quad (27b)$$

By bringing the value of the force deduced from the second relation to the first equation, we have

$$\mathbf{j}(\omega) = \left[\hat{\sigma}(\omega) - \frac{\sigma_0}{1 - i\omega \gamma^{-1}} \right] \mathcal{E}(\omega), \quad (28a)$$

with

$$\sigma_0 = \frac{C_{\parallel}^2 + C_{\perp}^2}{\gamma \varrho_\phi}. \quad (28b)$$

We find a Drude-like negative contribution to the effective conductivity. When the Fermi level lies within the electron gap we expect $\hat{\sigma}(0) \rightarrow 0$ ($\rho \rightarrow \infty$) at low temperatures, and it seems that the effective conductivity is dominated by this new negative correction given by

$$\sigma_0 = \frac{ne^2 \tau}{m_*},$$

with

$$m_* = \frac{\theta^2 \varrho_\phi}{n}, \quad (29)$$

where $\tau \equiv \gamma^{-1}$ is the momentum relaxation time. Note here the similarity of this expression with the sliding conductivity of an incommensurate charge-density wave [41], where m_* defined above plays the role of the effective mass of the sliding charge.

The important caveat is that nothing is really sliding here, and this apparent charge counterflow should be absent. The resolution of this paradox is that phasons are no longer soft, there must be a pinning gap ω_p in the spectrum, and we should replace the Drude-like factor $(\gamma - i\omega)^{-1}$ by $-i\omega/(\omega_p^2 - \omega^2 - i\omega\gamma)$ in these expressions. There is no DC transport in linear response, but there is a correction to the electric polarization density $\mathbf{P}(\omega) = -\mathbf{j}(\omega)/i\omega z_0$ (defined here per volume, with z_0 being the thickness of the bilayer) opposing the applied field, or in other words, a negative correction to the effective electric susceptibility,

$$\delta\chi_e(\omega) = -\frac{C_{\parallel}^2 + C_{\perp}^2}{\epsilon_0 z_0 \varrho_\phi (\omega_p^2 - \omega^2 - i\omega\gamma)} \quad (30a)$$

$$\xrightarrow{\omega \rightarrow 0} -\frac{ne^2}{\epsilon_0 z_0 m_* \omega_p^2}, \quad (30b)$$

where ϵ_0 is vacuum permittivity. The pinning gap is ultimately related to a smooth (so that the gap remains open) distortion of the moiré pattern under the application of an electric field. In this case the adiabatic approximation is ensured so long ω_p^{-1} is long compared to the timescale set by the electronic gap.

We can consider the alternative situation of a purely mechanical experiment/device in which the layers are free to slide ($\omega_p = 0$), but there are no electric contacts, so charge cannot flow, $\mathbf{j} = 0$. In this case, the constitutive relations in the $\omega = 0$ limit dictate that layers slide at a rate $\mathbf{v} = \mathbf{f}/\tilde{\gamma}\varrho$ with an enhanced friction parameter $\tilde{\gamma}$ given by

$$\tilde{\gamma} = \frac{\gamma}{1 - \sigma_0 \rho}, \quad (31)$$

where σ_0 is the *sliding conductivity* introduced before. Note that $1 \geq \sigma_0 \rho \geq 0$, hence, $\tilde{\gamma} > 0$ for thermodynamic stability Eq. (26).

This last result expresses that the friction between layers is effectively larger when the system is charged. As the layers slide, there is a pumping electromotive force perpendicular (in the case of twisted bilayer graphene) to the motion. If the system is isolated (disconnected from reservoirs/contacts), the pumped charge cannot leave the system, so a charge accumulation builds up. The associated voltage drop cancels the pumping electromotive force in the steady state. But this voltage drop produces an additional mechanical force opposing the original driving force, hence, modifying the relation between force and sliding velocity: one has to apply a larger force to slide at the same velocity. Quantum mechanically, the spectral flow linked to this charge accumulation implies the existence of edge states associated with the moiré pattern [26,42,43].

IV. DEPINNING FIELDS

The main result in Eq. (2) suggests that if external conditions do not prevent the sliding motion of the layers (the second scenario discussed in the previous section) an arbitrary small field should be able to drive this motion. In real devices, however, the presence of disorder implies a finite threshold that the driving force must overcome first. A model for the locked-to-sliding transition is beyond the linear-response theory presented here. The following is a rough estimate of the order of magnitude of the depinning fields in the same spirit as in the problem for charge-density waves [44,45].

In order to estimate the total pinning force opposing the driving field, I am going to neglect thermal fluctuations and consider only the static mechanical response to a quenched distribution of random forces acting on stacking configurations. The mechanical free energy is $\mathcal{U} + \int d\mathbf{r} \mathcal{V}_{\text{dis}}(\mathbf{r}, \delta\boldsymbol{\phi})$; the disorder potential $\mathcal{V}_{\text{dis}}(\mathbf{r}, \delta\boldsymbol{\phi})$ favors deviations of the stacking order at a given point \mathbf{r} from the one imposed by the moiré pattern and the mutual interaction between layers, therefore, pinning the relaxed texture $\boldsymbol{\phi}_0(\mathbf{r})$. We assume that disorder is weak in the sense that spatial variations of stacking fields are smooth compared to the moiré pitch. We can then expand to linear order in $\delta\boldsymbol{\phi}$, $\mathcal{V}_{\text{dis}}(\mathbf{r}, \delta\boldsymbol{\phi}) \approx -f_{\text{dis}}(\mathbf{r}) \cdot \delta\boldsymbol{\phi}$, where $f_{\text{dis}}(\mathbf{r})$ is some distribution of microscopic pinning forces. For simplicity, we model them with a Gaussian distribution with variance,

$$\langle f_i(\mathbf{r})f_j(\mathbf{r}') \rangle_{\text{dis}} = \overline{f_{\text{dis}}^2} \xi^2 \delta_{ij} \delta(\mathbf{r} - \mathbf{r}'). \quad (32)$$

The model can be understood as spatial distribution of pinning centers of characteristic force $(\overline{f_{\text{dis}}^2})^{1/2}$ coarse grained in a microscopic length ξ representing its characteristic range.

From general arguments for elastic media [46,47], the moiré pattern always breaks into finite domains regardless of the microscopic origin of disorder [33]. Beyond its characteristic size L_{pin} , the stacking configurations are no longer correlated and the cumulative effect of the microscopic pinning forces must stop. Due to their random orientation the total pinning force on the domain grows with the length, not the area. This opposes the driving force, Eq. (2) integrated over the area L_{pin}^2 . Consequently, there is always a finite strength of

the electric field that overcomes pinning,

$$\mathcal{E}_c = \frac{\xi}{L_{\text{pin}}} \sqrt{\frac{\overline{f_{\text{dis}}^2}}{C_{\parallel}^2 + C_{\perp}^2}}. \quad (33)$$

The size of the domains corresponds to the distance at which the spatial fluctuations in stackings exceed the microscopic length ξ . In linear response, taking the static limit $\omega = 0$ of the susceptibility in Eq. (20) and dropping the logarithm in the estimate of L_{pin} [33], we have

$$\mathcal{E}_c \approx \sqrt{\frac{3(\kappa_L^2 + \kappa_T^2)}{\pi}} \frac{a^2 \overline{f_{\text{dis}}^2} \xi}{8e\theta\kappa_L\kappa_T}, \quad (34)$$

where $\kappa_{L,T}$ is the stiffness of longitudinal and transverse phonon fluctuations and I have used the result for twisted bilayer graphene in Eq. (15).

Taking $\xi \sim a$ and disorder strength of the order of adhesion energies between graphene layers, $\xi(\overline{f_{\text{dis}}^2})^{1/2} \sim 4 \text{ meV}/\text{\AA}^2$ (the difference between AA and AB/BA stacking configurations [48]), and identifying $\kappa_L = \mu$, $\kappa_T = \lambda + 2\mu$, where $\lambda = 3.25 \text{ eV}/\text{\AA}^2$, $\mu = 9.57 \text{ eV}/\text{\AA}^2$ are graphene's Lamé coefficients [49], the collective pinning lengths are estimated in $L_{\text{pin}} \sim 500 \text{ nm}$, which is roughly the characteristic size of domains in the landscape of twist angle variations around the magic condition observed in experiment [50]. Bringing these numbers to the expression of the depinning field, we have $\mathcal{E}_c \sim 5 \text{ kV/cm}$ at the magic angle. Note, however, that, for the same disorder parameters, the depinning fields are smaller for larger twist angles, $\mathcal{E}_c \propto \theta^{-1}$.

Are these small or large? We can compare them with the depinning fields for charge-density waves. Naturally, these vary from one material to another depending on the amount of disorder, temperature, and other factors. In a typical system such as NbSe₃, threshold fields for the sliding conduction range from tens of mV/cm [51] to a few V/cm [52]. Threshold fields of few V/cm have been also reported recently for the axion insulator candidate (TaSe₄)₂I [53] and previously for a commensurate charge-density wave in a managanite [54]. We can conclude that the estimated \mathcal{E}_c , here, is, at least, two to three orders of magnitude larger than the typical threshold fields observed in sliding conduction [28] with the recent exception of a nearly commensurate 2D charge-density wave in 1T-TaS₂, which is as large as 1 kV/cm [55].

V. CONCLUSIONS

The constitutive relations written above describe the coupled response of a twisted Van der Waals bilayer against electric fields and layer-shear mechanical forces. These relations are general in the sense that they account also for intrinsic forces between layers responsible for lattice relaxation, pinning, and friction. Along with the resistivity ρ and the friction parameter γ , we must consider also new coefficients $C_{\parallel,\perp}$ describing reactive forces on stacking configurations exerted by an electric field when the moiré pattern is charged. From Onsager reciprocity, these

must be the same coefficients describing charge pumping by the sliding motion of one layer with respect to the other [23–25].

This new mechanical force has a geometrical origin. In agreement with Refs. [23–25], the coefficients $C_{\perp,\parallel}$ appearing in the lowest-order correction to the mechanical action can be expressed as integrals of a Berry curvature defined on the mixed space spanned by momenta and stacking configurations. In twisted bilayer graphene, $C_{\parallel} = 0$ due to C_2 symmetry and $C_{\perp} = -e\nu/\theta A_m$, where ν is the band filling measured from neutrality. This is strictly true for completely filled/empty bands, which is a consequence of a topological quantization in terms of four sliding Chern numbers defined on this mixed space [23–25]. The calculation for noninteger fillings including a self-consistent Hartree potential shows that C_{\perp} tracks the electron density for most fillings, although it is important to note that, in the presence of a Fermi surface, the adiabatic regime is not rigorously defined, and there must be corrections to the force in Eq. (2), including dissipative terms due to electron quasi-particle excitations. These processes introduce additional relaxation channels for the linear momentum of individual layers, and, hence, electronic contributions to interlayer friction.

The application of the constitutive relations shows that, when the relative position of the layers is pinned, there is still a negative correction to the electric polarization opposing the electric field. The reciprocal effect is an effective increase in the friction between layers when the system is charged and free to slide. This, however, might be challenging to probe in the laboratory due to the thermodynamic instability intrinsic to incommensurate layers.

It is important to stress that already in linear response thermodynamic stability [Eq. (26)] imposes a stringent condition for the observation of a topological Thouless pump in the sense that, when the chemical potential lies within the gap of the electron bands and $\rho \rightarrow \infty$ at low temperatures, the layers cannot be free to slide. In this regard, charged impurities may contribute to pin the moiré pattern in the same way as in Wigner crystals [56] provided that charge is more concentrated in some stacking areas within the moiré cell.

Finally, for a model of weak disorder compatible with the observed deviations in twist angles close to the magic-angle condition, the depinning fields for the sliding motion of the graphene layers are on the order of $\mathcal{E}_c \approx 5$ kV/cm. These are large if we compare them with typical depinning fields for incommensurate charge-density waves [28]. This probably constitutes the major limitation for the control of the stacking order by electric means.

ACKNOWLEDGMENTS

I am grateful to R. M. Fernandes and to D. Xiao for useful correspondence and to F. de Juan for pointing me to relevant literature on charge-density waves. Funding from the Spanish MCI/AEI/FEDER through Grant No. PID2021-128760NB-I00 is acknowledged.

APPENDIX A: SLIDING BERRY CURVATURE FROM EQ. (7)

The free Green's operator in the Bloch basis $|n, \mathbf{q}, \alpha\rangle$, where n is the band index and α represents the rest of quantum numbers (spin, valley, etc.), can be written as

$$\hat{G}_0(\omega, \mathbf{q}) = \sum_{n,\alpha} \left[\frac{\Theta[\varepsilon_{n,\alpha}(\mathbf{q}) - \mu]}{\hbar\omega + i0^+ - [\varepsilon_{n,\alpha}(\mathbf{q}) - \mu]} + \frac{\Theta[\mu - \varepsilon_{n,\alpha}(\mathbf{q})]}{\hbar\omega + i0^- - [\varepsilon_{n,\alpha}(\mathbf{q}) - \mu]} \right] |n, \mathbf{q}, \alpha\rangle \langle n, \mathbf{q}, \alpha|. \quad (\text{A1})$$

$\varepsilon_{n,\alpha}(\mathbf{q})$ is the band dispersion and $\Theta(x)$ is the Heaviside step function. Hereafter, the electronic Hamiltonian is assumed to be diagonal in α numbers. Equation (7) can be written as

$$\begin{aligned} \tilde{C}_{ij} = & \sum_{\alpha} \sum_{n_1, n_2} \int_{\text{mBZ}} \frac{d\mathbf{q}}{(2\pi)^2} \langle n_1, \mathbf{q}, \alpha | \partial_{\phi_j} \hat{H}_0 | n_2, \mathbf{q}, \alpha \rangle \langle n_2, \mathbf{q}, \alpha | \partial_{\phi_i} \hat{H}_0 | n_1, \mathbf{q}, \alpha \rangle \int_{-\infty}^{\infty} \frac{d\hbar\omega}{2\pi} \left(\frac{\Theta(\varepsilon_{n_1,\alpha}(\mathbf{q}) - \mu)}{\hbar\omega + i0^+ - (\varepsilon_{n_1,\alpha}(\mathbf{q}) - \mu)} \right. \\ & \left. + \frac{\Theta[\mu - \varepsilon_{n_1,\alpha}(\mathbf{q})]}{\hbar\omega + i0^- - [\varepsilon_{n_1,\alpha}(\mathbf{q}) - \mu]} \right)^2 \left(\frac{\Theta[\varepsilon_{n_2,\alpha}(\mathbf{q}) - \mu]}{\hbar\omega + i0^+ - [\varepsilon_{n_2,\alpha}(\mathbf{q}) - \mu]} + \frac{\Theta[\mu - \varepsilon_{n_2,\alpha}(\mathbf{q})]}{\hbar\omega + i0^- - [\varepsilon_{n_2,\alpha}(\mathbf{q}) - \mu]} \right). \end{aligned} \quad (\text{A2})$$

Only when the two poles lie at different halves of the complex plane the result of the integral in ω is different from 0. The result is

$$\begin{aligned} \tilde{C}_{ij} = & \sum_{\alpha} \sum_{n_1, n_2} \int_{\text{mBZ}} \frac{d\mathbf{q}}{(2\pi)^2} \frac{-2 \text{Im}[\langle n_1, \mathbf{q}, \alpha | \partial_{\phi_j} \hat{H}_0 | n_2, \mathbf{q}, \alpha \rangle \langle n_2, \mathbf{q}, \alpha | \partial_{\phi_i} \hat{H}_0 | n_1, \mathbf{q}, \alpha \rangle]}{[\varepsilon_{n_1,\alpha}(\mathbf{q}) - \varepsilon_{n_2,\alpha}(\mathbf{q})]^2} \Theta[\mu - \varepsilon_{n_2,\alpha}(\mathbf{q})] \Theta[\varepsilon_{n_1,\alpha}(\mathbf{q}) - \mu] \\ = & \sum_{\alpha, n} \int_{\text{mBZ}} \frac{d\mathbf{q}}{(2\pi)^2} \Omega_{q_i \phi_j}^{(n,\alpha)}(\mathbf{q}) \Theta[\mu - \varepsilon_{n,\alpha}(\mathbf{q})], \end{aligned} \quad (\text{A3})$$

where I have introduced the sliding Berry curvature [23–25],

$$\Omega_{q_i \phi_j}^{(n,\alpha)}(\mathbf{q}) = \sum_{n' \neq n} \frac{-2 \text{Im}[\langle n, \mathbf{q}, \alpha | \partial_{q_i} \hat{H}_0 | n', \mathbf{q}, \alpha \rangle \langle n', \mathbf{q}, \alpha | \partial_{\phi_j} \hat{H}_0 | n, \mathbf{q}, \alpha \rangle]}{[\varepsilon_{n,\alpha}(\mathbf{q}) - \varepsilon_{n',\alpha}(\mathbf{q})]^2}. \quad (\text{A4})$$

APPENDIX B: SELF-CONSISTENT HARTREE POTENTIAL

The Hartree potential (diagonal in sublattices and layers) reads

$$V_H(\mathbf{r}) = \int d\mathbf{r}' \frac{e^2}{4\pi\epsilon_0\epsilon_r|\mathbf{r}-\mathbf{r}'|} n(\mathbf{r}'), \quad (\text{B1})$$

where ϵ_r describes the dielectric environment. The electron density is periodic on the moiré pattern and, thus, admits a Fourier expansion of the form

$$n(\mathbf{r}) = \sum_{\{\mathbf{G}\}} n_{\mathbf{G}} e^{i\mathbf{G}\cdot\mathbf{r}}, \quad (\text{B2})$$

where $n_{\mathbf{G}}$'s are computed self-consistently from the Hartree bands $\epsilon_{n,\zeta}^H(\mathbf{q})$ and wave-functions $u_{n,\mathbf{q},\zeta}^H(\mathbf{r})$,

$$n_{\mathbf{G}} = 4 \sum_n \int_{\text{mBZ}} \frac{d\mathbf{q}}{(2\pi)^2} \rho_{\mathbf{G}}^{(n,+)}(\mathbf{q}) \Theta[\mu - \epsilon_{n,\zeta}^H(\mathbf{q})]. \quad (\text{B3})$$

The factor 4 comes from spin and valley degeneracies, and I have introduced the form factors,

$$\rho_{\mathbf{G}}^{(n,\zeta)}(\mathbf{q}) = \int d\mathbf{r} e^{-i\mathbf{G}\cdot\mathbf{r}} [u_{n,\zeta,\mathbf{q}}^H(\mathbf{r})]^* u_{n,\zeta,\mathbf{q}}^H(\mathbf{r}). \quad (\text{B4})$$

In the calculations of Fig. 3 the number of harmonics in the Fourier expansion of $n(\mathbf{r})$ was restricted to momenta \mathbf{G} in the first star of the moiré; $n_{\mathbf{G}}$ reduces then to the same real number for the six vectors due to D_6 symmetry. The bands in Fig. 3 were computed after determining this number in an iterative calculation with an error inferior to 1% for these two examples (errors never exceeded 2.5% in the calculations of Fig. 4). The appreciable distortion of the flat-band dispersion agrees well with similar calculations in the literature [37–40].

For the calculation of the matrix elements of $\partial_{\phi} \hat{\mathcal{H}}$ is important to emphasize again that all position-dependent terms in the Hamiltonian are a functional of the stacking configuration and, in particular, there is also a contribution from the Hartree term. The previous expressions for the Hartree potential were implicitly written in the coordinate frame defined by $\phi_0(\mathbf{r})$. Under an adiabatic change in stacking configurations the wave functions and, therefore, the form factors are transformed accordingly, $\rho_{\mathbf{G}}^{(n,\zeta)}(\mathbf{q}) \rightarrow e^{i\theta(\mathbf{G}\times\delta\phi)} \rho_{\mathbf{G}}^{(n,\zeta)}(\mathbf{q})$. Thus, the Hartree potential can be written as a functional of the stacking field as

$$V_H(\mathbf{r}) \equiv V_H[\phi(\mathbf{r})] = \sum_i e^{i\mathbf{g}_i\cdot\phi(\mathbf{r})} \frac{n_{\mathbf{G}_i} e^2}{2\epsilon_0\epsilon_r|\mathbf{G}_i|}. \quad (\text{B5})$$

APPENDIX C: QUANTIZATION OF THE FORCE COEFFICIENTS AND RELATION TO THE SYMMETRIES OF THE MODEL

Consider the expression of the force coefficients in Eq. (11) in terms of the sliding Berry curvature in Eq. (A4). The latter does not depend on the stacking deviation $\delta\phi$, what is ultimately rooted in the fact that the two layers are incommensurate to each other. Assuming that the Fermi level lies within a gap and accounting for spin and valley degeneracies, we can write

$$C_{ij} = \frac{4e}{A_c} \sum_{n \in \text{occ}} \int_{A_c} d\phi \int_{\text{mBZ}} \frac{d\mathbf{q}}{(2\pi)^2} \Omega_{q_i\phi_j}^{(n,+)}(\mathbf{q}), \quad (\text{C1})$$

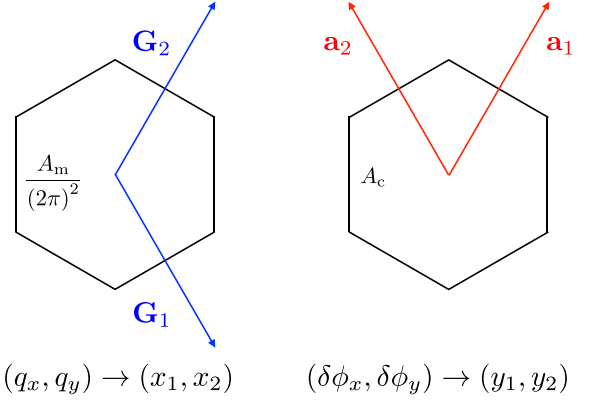


FIG. 5. Parametrization of momenta and stacking configurations. The primitive vectors in momentum space are shown in blue and for stacking fields in red.

where the sum is in occupied bands and the additional integration is in stacking configurations defined mod a Bravais vector of graphene's lattice; A_c is the area of graphene's unit cell.

In order to see the topological origin of the force coefficients in this case, it is convenient to change variables to dimensionless units $x_{1,2}, y_{1,2} \in [0, 1)$ parametrizing, respectively, momenta and stackings as

$$\mathbf{q} = \sum_{\alpha=1,2} x_{\alpha} \mathbf{G}_{\alpha}, \quad (\text{C2a})$$

$$\delta\phi = \sum_{\alpha=1,2} y_{\alpha} \mathbf{a}_{\alpha}. \quad (\text{C2b})$$

Here, $\mathbf{a}_{1,2}$ and $\mathbf{G}_{1,2}$ are primitive vectors of the graphene's Bravais lattice and the moiré reciprocal lattice. Without loss of generality, I choose the primitive vectors as indicated in Fig. 5. Changing variables in the integration measure and noting that the Berry curvature in the new variables is the pullback of the curvature in the old variables, we can write

$$C_{ij} = \frac{4e}{A_m} \sum_{\alpha,\beta} \frac{[\mathbf{A}_{\alpha}]_i [\mathbf{g}_{\beta}]_j}{2\pi} \sum_{n \in \text{occ}} c_{\alpha,\beta}^{(n,+)}, \quad (\text{C3})$$

where $\mathbf{A}_{1,2}$ and $\mathbf{g}_{1,2}$ are dual to the primitive vectors, $\mathbf{A}_{\alpha} \cdot \mathbf{G}_{\beta} = \mathbf{a}_{\alpha} \cdot \mathbf{g}_{\beta} = 2\pi \delta_{\alpha,\beta}$, and $c_{\alpha,\beta}^{(n,+)}$ are Chern numbers defined on the mixed space of momenta and stackings,

$$c_{\alpha,\beta}^{(n,+)} = \frac{1}{2\pi} \int_0^1 dx_{\alpha} \int_0^1 dy_{\beta} \Omega_{x_{\alpha}y_{\beta}}^{(n,+)} \in \mathbb{Z}. \quad (\text{C4})$$

Specifically, the force coefficients introduced in the main text can be written as (repeated latin indices are summed)

$$C_{\parallel} = \frac{C_{ii}}{2} = \frac{4e}{A_m} \sum_{\alpha,\beta} \frac{\mathbf{A}_{\alpha} \cdot \mathbf{g}_{\beta}}{2\pi} \sum_{n \in \text{occ}} \frac{c_{\alpha,\beta}^{(n,+)}}{2}, \quad (\text{C5a})$$

$$C_{\perp} = \epsilon_{ji} \frac{C_{ij}}{2} = \frac{4e}{A_m} \sum_{\alpha,\beta} \frac{[\mathbf{g}_{\beta} \times \mathbf{A}_{\alpha}]_z}{2\pi} \sum_{n \in \text{occ}} \frac{c_{\alpha,\beta}^{(n,+)}}{2}. \quad (\text{C5b})$$

In the case of twisted bilayer graphene we have $\mathbf{A}_\alpha = \mathbf{a}_\alpha \times \hat{\mathbf{z}}/\theta$ with the previous choice of primitive vectors. The previous formulas reduce to

$$\begin{aligned} C_\perp &= -\frac{4e}{A_m\theta} \sum_{\alpha,\beta} \frac{\mathbf{a}_\alpha \cdot \mathbf{g}_\beta}{2\pi} \sum_{n \in \text{occ}} \frac{c_{\alpha,\beta}^{(n,+)}}{2} \\ &= -\frac{4e}{A_m\theta} \sum_{n \in \text{occ}} \frac{c_{1,1}^{(n,+)} + c_{2,2}^{(n,+)}}{2} = -\frac{4e}{A_m\theta} \sum_{n \in \text{occ}} c_{1,1}^{(n,+)}, \end{aligned} \quad (\text{C6a})$$

$$\begin{aligned} C_\parallel &= -\frac{4e}{A_m\theta} \sum_{\alpha,\beta} \frac{[\mathbf{a}_\alpha \times \mathbf{g}_\beta]_z}{2\pi} \sum_{n \in \text{occ}} \frac{c_{\alpha,\beta}^{(n,+)}}{2} \\ &= \frac{4e}{A_m\theta} \sum_{n \in \text{occ}} \frac{c_{1,1}^{(n,+)} - c_{2,2}^{(n,+)} - 2c_{1,2}^{(n,+)} + 2c_{2,1}^{(n,+)}}{\sqrt{3}} = 0. \end{aligned} \quad (\text{C6b})$$

In these expressions, we have used that labels 1 and 2 can be exchanged under C_2 symmetries within the plane of the

structure, i.e., $c_{1,1}^{(n,+)} = c_{2,2}^{(n,+)}$ and $c_{1,2}^{(n,+)} = c_{2,1}^{(n,+)}$. We obtain then that C_\parallel is 0 by symmetry and C_\perp is quantized in units of $\frac{4e}{A_m\theta}$ in agreement with the discussion in Sec. II.

What happens if in-plane C_2 symmetries are broken? If the gaps between the flat bands and the rest of the spectrum are not closed and reopened, then the sum of the sliding Chern numbers over occupied bands cannot change. However, the geometrical prefactors change if the moiré pattern is modified accordingly. For example, if the twist is accompanied by a change in lattice parameters (such as in graphene on boron nitride) given by a dimensionless number ε , which can be understood as a biaxial heterostrain ($\varepsilon = 0$ for the same lattice constants), then,

$$\mathbf{A}_\alpha = \frac{\varepsilon \mathbf{a}_\alpha + \theta \mathbf{a}_\alpha \times \hat{\mathbf{z}}}{\varepsilon^2 + \theta^2}. \quad (\text{C7})$$

We can see from this and previous expressions that even if the sum of the sliding Chern numbers do not change, there is a nonzero longitudinal force $C_\parallel \propto \varepsilon/(\varepsilon^2 + \theta^2)$ coming from the geometrical prefactor.

-
- [1] J. M. B. Lopes dos Santos, N. M. R. Peres, and A. H. Castro Neto, *Phys. Rev. Lett.* **99**, 256802 (2007).
- [2] E. Khalaf, A. J. Kruchkov, G. Tarnopolsky, and A. Vishwanath, *Phys. Rev. B* **100**, 085109 (2019).
- [3] E. Suárez Morell, J. D. Correa, P. Vargas, M. Pacheco, and Z. Barticevic, *Phys. Rev. B* **82**, 121407(R) (2010).
- [4] R. Bistritzer and A. H. MacDonald, *Proc. Natl. Acad. Sci. USA* **108**, 12233 (2011).
- [5] Y. Cao, V. Fatemi, S. Fang, K. Watanabe, T. Taniguchi, E. Kaxiras, and P. Jarillo-Herrero, *Nature (London)* **556**, 43 (2018).
- [6] Y. Cao, V. Fatemi, A. Demir, S. Fang, S. L. Tomarken, J. Y. Luo, J. D. Sanchez-Yamagishi, K. Watanabe, T. Taniguchi, E. Kaxiras, R. C. Ashoori, and P. Jarillo-Herrero, *Nature (London)* **556**, 80 (2018).
- [7] M. Yankowitz, S. Chen, H. Polshyn, Y. Zhang, K. Watanabe, T. Taniguchi, D. Graf, A. F. Young, and C. R. Dean, *Science* **363**, 1059 (2019).
- [8] A. L. Sharpe, E. J. Fox, A. W. Barnard, J. Finney, K. Watanabe, T. Taniguchi, M. A. Kastner, and D. Goldhaber-Gordon, *Science* **365**, 605 (2019).
- [9] X. Lu, P. Stepanov, W. Yang, M. Xie, M. A. Aamir, I. Das, C. Urgell, K. Watanabe, T. Taniguchi, G. Zhang, A. Bachtold, A. H. MacDonald, and D. K. Efetov, *Nature (London)* **574**, 653 (2019).
- [10] A. Kerelsky, L. J. McGilly, D. M. Kennes, L. Xian, M. Yankowitz, S. Chen, K. Watanabe, T. Taniguchi, J. Hone, C. Dean, A. Rubio, and A. N. Pasupathy, *Nature (London)* **572**, 95 (2019).
- [11] Y. Xie, B. Lian, B. Jäck, X. Liu, C.-L. Chiu, K. Watanabe, T. Taniguchi, B. A. Bernevig, and A. Yazdani, *Nature (London)* **572**, 101 (2019).
- [12] Y. Jiang, X. Lai, K. Watanabe, T. Taniguchi, K. Haule, J. Mao, and E. Y. Andrei, *Nature (London)* **573**, 91 (2019).
- [13] Y. Choi, J. Kemmer, Y. Peng, A. Thomson, H. Arora, R. Polski, Y. Zhang, H. Ren, J. Alicea, G. Refael, F. von Oppen, K. Watanabe, T. Taniguchi, and S. Nadj-Perge, *Nat. Phys.* **15**, 1174 (2019).
- [14] M. Serlin, C. Tschirhart, H. Polshyn, Y. Zhang, J. Zhu, K. Watanabe, T. Taniguchi, L. Balents, and A. Young, *Science* **367**, 900 (2020).
- [15] U. Zondiner, A. Rozen, D. Rodan-Legrain, Y. Cao, R. Queiroz, T. Taniguchi, K. Watanabe, Y. Oreg, F. von Oppen, A. Stern, E. Berg, P. Jarillo-Herrero, and S. Ilani, *Nature (London)* **582**, 203 (2020).
- [16] D. Wong, K. P. Nuckolls, M. Oh, B. Lian, Y. Xie, S. Jeon, K. Watanabe, T. Taniguchi, B. A. Bernevig, and A. Yazdani, *Nature (London)* **582**, 198 (2020).
- [17] Y. Cao, D. Rodan-Legrain, J. M. Park, N. F. Q. Yuan, K. Watanabe, T. Taniguchi, R. M. Fernandes, L. Fu, and P. Jarillo-Herrero, *Science* **372**, 264 (2021).
- [18] A. Rozen, J. M. Park, U. Zondiner, Y. Cao, D. Rodan-Legrain, T. Taniguchi, K. Watanabe, Y. Oreg, A. Stern, E. Berg, P. Jarillo-Herrero, and S. Ilani, *Nature (London)* **592**, 214 (2021).
- [19] Y. Saito, F. Yang, J. Ge, X. Liu, T. Taniguchi, K. Watanabe, J. Li, E. Berg, and A. F. Young, *Nature (London)* **592**, 220 (2021).
- [20] X. Hu, T. Hyart, D. I. Pikulin, and E. Rossi, *Phys. Rev. Lett.* **123**, 237002 (2019).
- [21] F. Xie, Z. Song, B. Lian, and B. A. Bernevig, *Phys. Rev. Lett.* **124**, 167002 (2020).
- [22] A. Julku, T. J. Peltonen, L. Liang, T. T. Heikkilä, and P. Törmä, *Phys. Rev. B* **101**, 060505(R) (2020).
- [23] M. Fujimoto, H. Koschke, and M. Koshino, *Phys. Rev. B* **101**, 041112(R) (2020).
- [24] Y. Su and S.-Z. Lin, *Phys. Rev. B* **101**, 041113(R) (2020).
- [25] Y. Zhang, Y. Gao, and D. Xiao, *Phys. Rev. B* **101**, 041410(R) (2020).
- [26] M. Fujimoto and M. Koshino, *Phys. Rev. B* **103**, 155410 (2021).
- [27] D. J. Thouless, *Phys. Rev. B* **27**, 6083 (1983).
- [28] G. Grüner, *Rev. Mod. Phys.* **60**, 1129 (1988).
- [29] The convention is that the top layer is rotated anticlockwise with respect to the bottom layer an angle θ .

- [30] M. Koshino and Y.-W. Son, *Phys. Rev. B* **100**, 075416 (2019).
- [31] H. Ochoa, *Phys. Rev. B* **100**, 155426 (2019).
- [32] I. Maity, M. H. Naik, P. K. Maiti, H. R. Krishnamurthy, and M. Jain, *Phys. Rev. Res.* **2**, 013335 (2020).
- [33] H. Ochoa and R. M. Fernandes, *Phys. Rev. Lett.* **128**, 065901 (2022).
- [34] Q. Gao and E. Khalaf, *Phys. Rev. B* **106**, 075420 (2022).
- [35] R. Samajdar, Y. Teng, and M. S. Scheure, *Phys. Rev. B* **106**, L201403 (2022).
- [36] M. Koshino, N. F. Q. Yuan, T. Koretsune, M. Ochi, K. Kuroki, and L. Fu, *Phys. Rev. X* **8**, 031087 (2018).
- [37] L. Rademaker and P. Mellado, *Phys. Rev. B* **98**, 235158 (2018).
- [38] F. Guinea and N. R. Walet, *Proc. Natl. Acad. Sci. USA* **115**, 13174 (2018).
- [39] T. Cea, N. R. Walet, and F. Guinea, *Phys. Rev. B* **100**, 205113 (2019).
- [40] L. Rademaker, D. A. Abanin, and P. Mellado, *Phys. Rev. B* **100**, 205114 (2019).
- [41] P. A. Lee, T. M. Rice, and P. W. Anderson, *Solid State Commun.* **14**, 703 (1974).
- [42] M. Fleischmann, R. Gupta, D. Weckbecker, W. Landgraf, O. Pankratov, V. Meded, and S. Shallcross, *Phys. Rev. B* **97**, 205128 (2018).
- [43] J. Liu, J. Liu, and X. Dai, *Phys. Rev. B* **99**, 155415 (2019).
- [44] H. Fukuyama and P. A. Lee, *Phys. Rev. B* **17**, 535 (1978).
- [45] P. A. Lee and T. M. Rice, *Phys. Rev. B* **19**, 3970 (1979).
- [46] Y. Imry and S.-K. Ma, *Phys. Rev. Lett.* **35**, 1399 (1975).
- [47] A. I. Larkin and Yu. N. Ovchinnikov, *J. Low Temp. Phys.* **34**, 409 (1979).
- [48] S. Carr, D. Massatt, S. B. Torrisi, P. Cazeaux, M. Luskin, and E. Kaxiras, *Phys. Rev. B* **98**, 224102 (2018).
- [49] K. V. Zakharchenko, M. I. Katsnelson, and A. Fasolino, *Phys. Rev. Lett.* **102**, 046808 (2009).
- [50] A. Uri, S. Grover, Y. Cao, J. Crosse, K. Bagani, D. Rodan-Legrain, Y. Myasoedov, K. Watanabe, T. Taniguchi, P. Moon, M. Koshino, P. Jarillo-Herrero, and E. Zeldov, *Nature (London)* **581**, 47 (2020).
- [51] R. M. Fleming and C. C. Grimes, *Phys. Rev. Lett.* **42**, 1423 (1979).
- [52] M. Ido, Y. Okajima, H. Wakimoto, and M. Oda, *J. Phys. Soc. Jpn.* **56**, 2503 (1987).
- [53] J. Gooth, B. Bradlyn, S. Honnali, C. Schindler, N. Kumar, J. Noky, Y. Qi, C. Shekhar, Y. Sun, Z. Wang, B. A. Bernevig, and C. Felse, *Nature (London)* **575**, 315 (2019).
- [54] S. Cox, J. Singleton, R. D. McDonald, A. Migliori, and P. B. Littlewood, *Nature Mater.* **7**, 25 (2008).
- [55] A. Mohammadzadeh, A. Rehman, F. Kargar, S. Romyantsev, J. M. Smulko, W. Knap, R. K. Lake, and A. A. Balandin, *Appl. Phys. Lett.* **118**, 223101 (2021).
- [56] I. M. Ruzin, S. Marianer, and B. I. Shklovskii, *Phys. Rev. B* **46**, 3999 (1992).